PAPER

Multiferroicity and phase diagram of ferro-rotational magnet $RbFe(SO_4)_2$

IOP Publishing Journal of Physics: Condensed Matter
J. Phys.: Condens. Matter **37** (2025) 175701 (7pp) https://doi.org/10.1088/1361-648X/adc064

Multiferroicity and phase diagram of ferro-rotational magnet $RbFe(SO_4)_2$

Junjie Yang[1,*], Dimuthu Obeysekera[1], William Ratcliff[2,3], Lu Li[4], Sabine N Neal[5,6], Janice L Musfeldt[5,6] and Shinichiro Yano[7]

[1] Department of Physics, New Jersey Institute of Technology, Newark, NJ 07102, United States of America
[2] NIST Center for Neutron Research, National Institute of Standards and Technology, Gaithersburg, MD 20899, United States of America
[3] Department of Materials Science and Engineering, Department of Physics, University of Maryland, College Park, MD 20742, United States of America
[4] Department of Physics, University of Michigan, 450 Church St, Ann Arbor, MI 48109, United States of America
[5] Department of Chemistry, University of Tennessee, Knoxville, TN 37996, United States of America
[6] Department of Physics and Astronomy, University of Tennessee, Knoxville, TN 37996, United States of America
[7] National Synchrotron Radiation Research Center, Hsinchu 30077, Taiwan

E-mail: jyang@njit.edu

Received 6 January 2025, revised 22 February 2025
Accepted for publication 13 March 2025
Published 27 March 2025

Abstract

Ferro-rotational magnet $RbFe(SO_4)_2$ has attracted attention for its stable ferro-rotational phase and electric-field-controlled magnetic chirality. This work presents the multiferroic properties and H–T phase diagram of $RbFe(SO_4)_2$, which have been underexplored. Our measurements of magnetic susceptibility, ferroelectric polarization, and dielectric constant under various magnetic fields reveal four distinct phases: (I) a ferroelectric and helical magnetic phase below 4 K and 6 T, (II) a paraelectric and collinear magnetic phase below 4 K and above 6 T, (III) a paraelectric and non-collinear magnetic phase below 4 K and above 9 T, and (IV) a paraelectric and paramagnetic above 4 K. This study clarifies the multiferroic behavior and H–T phase diagram of $RbFe(SO_4)_2$, providing valuable insights into ferro-rotational magnets.

Keywords: multiferroic, polarization, ferro-rotation, phase diagram

1. Introduction

Ferro-rotational materials, where atomic polyhedra such as SO_4 exhibit spontaneous ordering of crystallographic rotational distortions in either a clockwise (CW) or counter CW (CCW) direction, lead to the emergence of an axial-vector order parameter known as ferro-rotation across large spatial dimensions [1–12]. Ferro-rotational materials and orders have gained significant attention due to their unique material functionalities. For instance, the combination of ferro-rotational order with chiral helical spin order can result in multiferroicity, which in turn offers the potential to control magnetic order through an electric field [2, 12]. Among the various ferro-rotational magnets, $RbFe(SO_4)_2$ has emerged as a focal point of recent research [8, 13, 14]. Coherent structural excitations of the Rb metal monolayer have been observed in this compound [14]. Compared to the isostructural $RbFe(MoO_4)_2$ crystal, $RbFe(SO_4)_2$ exhibits a significantly higher ferro-rotational transition temperature (T_{FR}) of around 573 K, while the T_{FR} of $RbFe(MoO_4)_2$ is only about 190 K [5, 13]. Moreover, neutron diffraction experiments on $RbFe(SO_4)_2$ have confirmed the presence of a chiral helical magnetic structure below 4 K [13]. Additionally, ferroelectric polarization

* Author to whom any correspondence should be addressed.

and dielectric constant measurements have verified its multiferroicity at zero magnetic fields [13]. Notably, polarized neutron diffraction experiments have demonstrated that external electric fields can manipulate the magnetic chirality in the $RbFe(SO_4)_2$ crystals [13].

While the multiferroicity of $RbFe(SO_4)_2$ at zero magnetic fields has been documented, how the multiferroicity evolves under external magnetic fields and the corresponding magnetic field-temperature (H–T) phase diagram remains unexplored. In this work, we present the multiferroic properties and the H–T phase diagram of $RbFe(SO_4)_2$. Our measurements of magnetic susceptibility as a function of temperature (χ–T), magnetization as a function of magnetic field (M–H), ferroelectric polarization as a function of temperature (P–T), and dielectric constant as a function of temperature (ε_r–T) at various magnetic fields reveal four distinct phases in the H–T phase diagram: (I) a ferroelectric and magnetic chiral helical phase, (II) a paraelectric and magnetic collinear phase, (III) a paraelectric and magnetic non-collinear phase, and (IV) a paraelectric and paramagnetic phase. The M–H curve at 1.8 K shows that as the magnetic field increases, the chiral helical magnetic structure first changes to a collinear achiral magnetic structure at 6 T, followed by a plateau between 6 and 9 T. Above 9 T, the magnetic structure likely evolves to an achiral non-collinear configuration. This study elucidates the multiferroic properties, magnetically-driven transitions, and the H–T phase diagram of $RbFe(SO_4)_2$, providing valuable insights into the exotic physical properties of this ferro-rotational system.

2. Results and discussions

The $RbFe(SO_4)_2$ single crystals were grown using the hydrothermal method [13]. Figures 1(A) and (B) illustrate the room-temperature crystal structure (space group $P\bar{3}$) of $RbFe(SO_4)_2$, as determined by our previous synchrotron x-ray diffraction experiments [13]. The crystal structure consists of alternating layers of SO_4 tetrahedra, FeO_6 octahedra, and Rb ions. In $RbFe(SO_4)_2$, the SO_4 tetrahedra exhibits a CCW or CW rotation around the c-axis, resulting in the ferro-rotational order. This ferro-rotational order breaks two mirror symmetries in the ab-plane of the $RbFe(SO_4)_2$ crystals while maintaining centrosymmetry. The centrosymmetric nature of $RbFe(SO_4)_2$ is further confirmed by our infrared absorption and Raman spectroscopy results in figure 1(C). In centrosymmetric materials, the mutual exclusion principle dictates that vibrational modes active in infrared are not active in Raman, and vice versa. There is no overlap between the infrared absorption and Raman spectra, confirming that $RbFe(SO_4)_2$ is centrosymmetric at room temperature.

It is unclear whether any structural transitions occur below room temperature. To address this, we conducted neutron diffraction experiments on an $RbFe(SO_4)_2$ single crystal from 280 to 2 K using the BT4 diffractometer at the NIST Center for Neutron Research. Figure 1(D) presents a contour map of the intensity of the (110) nuclear peak as a function of temperature and 2θ angles, while figure 1(E) shows the contour map for the (003) nuclear peak. In these maps, red indicates the highest intensity and blue the lowest. No peak splitting or significant changes in peak intensity were observed between 280 and 5 K for both the (110) and (003) peaks, suggesting that a long-range structural phase transition is unlikely in this temperature range. However, the 2θ angles for both peaks shift to higher values as temperature decreases, indicating that the lattice parameters a and c contract upon cooling.

We extracted the temperature dependence of the a, c lattice parameter, and the unit cell volume V, as shown in figures 1(F)–(H). All three parameters—a, c, and V—decrease with decreasing temperature, which is attributed to thermal contraction. Notably, from 280 to 5 K, the a lattice parameter changes by only 0.2%, while the c lattice parameter changes by 1%, five times more. This is characteristic of a two-dimensional (2D) lattice structure. It has been suggested that the temperature dependence of the c lattice parameter in a 2D material (such as graphite) can be fitted using a polynomial function: $c(T) = c_0 + c_1T^2 + c_2T^3 + c_3T^4$ [15]. For $RbFe(SO_4)_2$, the fitted parameters are $c_0 = 8.19$, $c_1 = 2.72 \times 10^{-6}$, $c_2 = -8.77 \times 10^{-9}$, and $c_3 = 1.06 \times 10^{-11}$. The coefficients c_1, c_2, and c_3 are about an order of magnitude larger than those for graphite [15], indicating a more pronounced thermal contraction and stronger interlayer van de Waals forces in $RbFe(SO_4)_2$. The temperature dependences of a and V can also be fitted with a similar polynomial, as indicated by the red curves in figures 1(F) and (H). An additional interesting feature is that below 4 K, both the c lattice parameter (see inset of figure 1(G)) and the unit cell volume V show a significant drop, which may be related to magnetic exchange interactions between the 2D layers. The c lattice parameter drops from 8.195 Å at 4 K to 8.188 Å at 1.6 K. In contrast, the a lattice parameter remains nearly unchanged across the magnetic ordering temperature $T_N \sim 4$ K. Despite the possibility that the interlayer van der Waals forces in $RbFe(SO_4)_2$ are stronger than those in the well-known 2D graphite, the temperature dependence of the c and a lattice parameters still suggests that $RbFe(SO_4)_2$ is an excellent 2D layered material.

Given the triangular arrangement of magnetic Fe^{3+} ions and the 2D nature of the lattice structure, $RbFe(SO_4)_2$ is expected to exhibit strong magnetic frustration. To investigate this, we measured the χ–T curve from 5 to 300 K, as shown on the left axis of figure 2(A). The $1/\chi$–T curve is also plotted on the right axis (in blue). We fitted the high-temperature region (150–300 K) of the $1/\chi$–T curve using the Curie–Weiss law: $1/\chi = (T-\theta_{CW})/C$. The Curie–Weiss temperature $\theta_{CW} \sim -22.2$ K and Curie–Weiss constant $C \sim 4.365$ were obtained from the fit. The value of θ_{CW} is significantly higher than the Néel temperature $T_N \sim 4$ K, confirming strong magnetic frustration, with a frustration ratio of $f = \theta_{CW}/T_N = 5.55$. The Curie–Weiss temperature can be further analyzed to determine J, the effective intralayer exchange coupling constant, using the equation $\theta_{CW} = -zJS(S+1)/3$. In this equation, $S = 5/2$ for Fe^{3+} ions, and $z = 6$ represents the number of nearest neighbors. With $\theta_{CW} = -22.2$ K, we calculate $J = 1.27$ K for our sample. The Curie–Weiss constant can be further analyzed to determine μ_{eff}, the effective magnetic moment of Fe^{3+} ions, using the equation $\mu_{eff} = 2.828\sqrt{C}$.

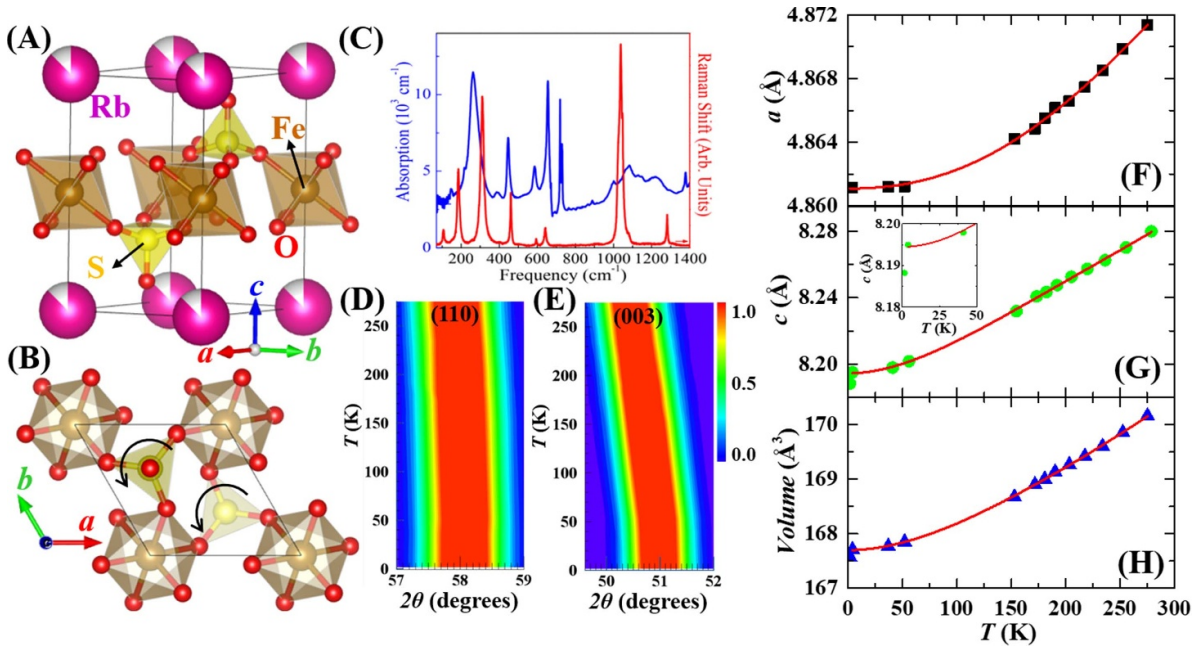

Figure 1. (A) Room-temperature crystal structure of $RbFe(SO_4)_2$. (B) Crystal structure of $RbFe(SO_4)_2$ in the *ab* plane, with black arrows highlighting the ferro-rotational distortions of SO_4, which break the mirror reflection symmetries in the *ab* plane. (C) Infrared absorption (blue) and Raman shifts (red) of an $RbFe(SO_4)_2$ crystal at room temperature. (D) Contour map of the neutron diffraction intensity for the (110) nuclear peak as a function of temperature and 2θ angles. (E) Contour map of the neutron diffraction intensity for the (003) nuclear peak. (F) Temperature dependence of the *a* lattice parameter with the fitted curve shown in red. (G) Temperature dependence of the *c* lattice parameter with the fitted curve shown in red. The inset provides a close-up view of the data at low temperatures. (H) Temperature dependence of the volume *V* with the fitted curve shown in red. For all the *a, c*, and *V* parameters, their uncertainties are smaller than the symbol size.

With $C \sim 4.365$, we calculate $\mu_{\text{eff}} = 5.909\ \mu_B$ which is very close to the theoretical value for Fe^{3+} ions.

The ground state of a 2D magnetic triangular lattice is characterized by moments aligned in the *ab* plane, forming a 120° configuration. Additionally, the ferro-rotational order breaks the two mirror symmetries in the *ab* plane, potentially causing the 120° configurations between neighboring layers to rotate around the *c*-axis, resulting in a chiral helical magnetic structure at zero magnetic fields [13]. To explore how this chiral helical magnetic structure evolves under external magnetic fields, we measured the χ–*T* curves from 2 to 8 K under various magnetic fields, with the fields applied along the *ab* plane of $RbFe(SO_4)_2$. As shown in figure 2(B), with increasing magnetic field strength, the antiferromagnetic transition temperature T_N shifts to lower values and is no longer visible at 6 T within our measured temperature range. As T_N is suppressed, a second transition at a slightly higher temperature emerges. This second transition shows a slight decreasing trend from 6 to 9 T, as seen in figure 2(B). These results suggest the emergence of a new magnetic phase in the external magnetic field range of 6–9 T.

To further confirm the magnetic field-induced transitions in $RbFe(SO_4)_2$, we measured the *M*–*H* curves from 0 to 14 T at various temperatures, with the field applied along the *ab* plane, as shown in figure 2(C). At 1.8 K, a plateau and two magnetic field-induced transitions are observed at $H_{c1} \sim 6$ T and $H_{c2} \sim 9$ T in the *M*–*H* curve. These transitions are more clearly visible in the first-order derivative *dM/dH*, as shown in figure 2(D). At 1.8 K, two sharp peaks are observed at 6 and 9 T in the *dM/dH* curve. As the temperature increases, the peak at 6 T (H_{c1}) shifts to a lower field, while the peak at 9 T (H_{c2}) remains unchanged. By 5 K, in the paramagnetic phase, both peaks at 6 and 9 T disappear in the *dM/dH* curve. The plateau in the *M*–*H* curve and the two peaks in the *dM/dH* curve are characteristic of a 2D triangular layered antiferromagnetic system [1, 12, 16–19]. It has been proposed that spin fluctuations play a crucial role in stabilizing the magnetization plateau [20, 21]. At higher temperatures, spin fluctuations are expected to become more pronounced, leading to a lower H_{c1}, which allows the plateau to remain stable over a broader range of magnetic fields. On the other hand, the magnetic structure exits the plateau state at H_{c2}, where the magnetic field energy becomes dominant. As a result, H_{c2} exhibits weak temperature dependence. We also performed *M*–*H* measurements with the magnetic field applied along the *c*-axis at 1.8 K, as shown in the inset of figure 2(C). With $H \parallel c$, the plateau in the *M*–*H* curve is absent. This is likely due to the strong single-ion anisotropy, which induces easy-plane anisotropy. As a result, when $H \parallel c$, the *M*–*H* curve remains linear.

Based on our previous neutron diffraction study of the magnetic structure in $RbFe(SO_4)_2$ under zero magnetic field, the magnetic ground state is a chiral helical 120° structure (Phase I) [13]. As the magnetic field increases, the spins likely deviate from the 120° configuration, transitioning to an antiparallel alignment, resulting in a ferrimagnetic state (Phase II) and an achiral collinear magnetic structure, as shown in the inset

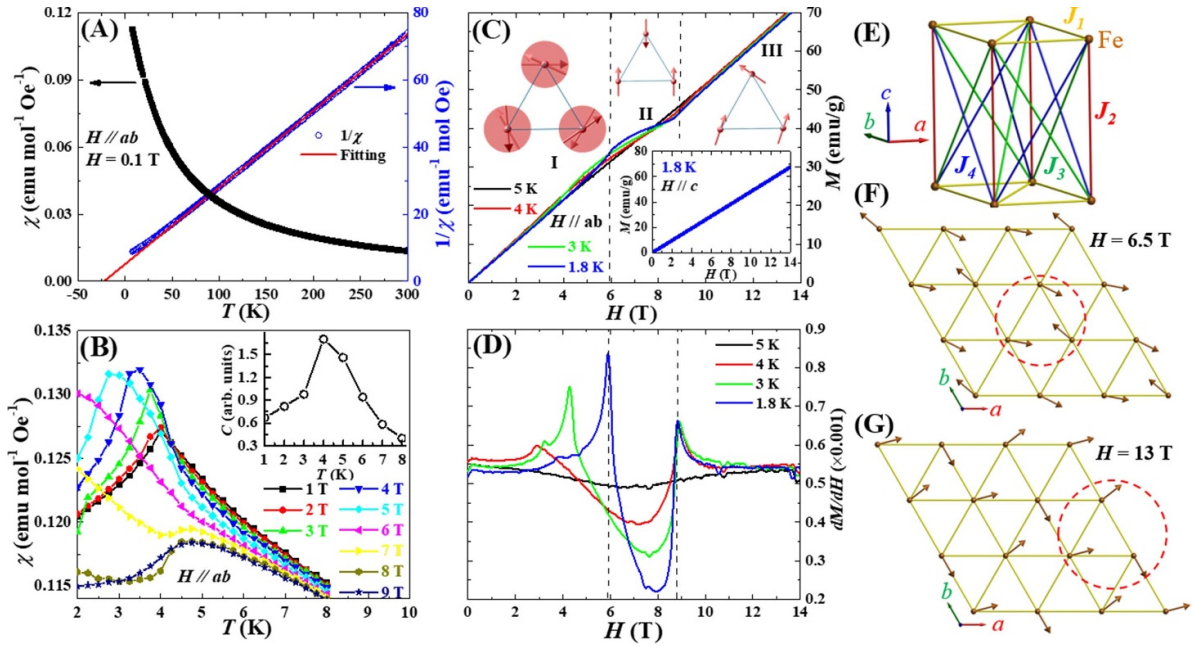

Figure 2. (A) Magnetic susceptibility as a function of temperature (χ–T) from 5 to 300 K for a $RbFe(SO_4)_2$ single crystal (left axis, black curve). The blue curve represents $1/\chi$–T, and the red solid line indicates the fitted data. (B) χ–T curves measured from 2 to 8 K under various magnetic fields. The inset shows the theoretically calculated temperature dependence of specific heat. (C) Magnetization as a function of magnetic field (M–H) measured at different temperatures. Dashed lines mark the phase boundary, and the insets depict the corresponding magnetic structures. The inset shows the M–H curve measured at 1.8 K with $H \,//\, c$. (D) First-order derivative dM/dH of the M–H curves shown in (C), with dashed lines marking the phase boundary. All magnetic susceptibility and magnetic moment measurements were taken with $H//ab$. (E) The illustration of the various exchange coupling constants in the adjacent Fe^{3+} triangular layers. Optimized magnetic structure with a 6.5 T (F) and 13 T (G) magnetic field applied along the a-axis. The red circles in (F) and (G) highlight the magnetic structures within a single unit cell for Phase II and Phase III, respectively.

of figure 2(C). Further increasing the magnetic field likely aligns the spins more in the direction of the field, distorting them into an achiral noncollinear magnetic structure (Phase III), also illustrated in the inset of figure 2(C). To validate that the magnetic structures of Phase II and Phase III are energetically favorable, we consider the following spin-Hamiltonian (per layer):

$$\begin{aligned}\mathcal{H} = & J_1 \sum_{\langle i,j \rangle} \vec{S}_{i,p} \cdot \vec{S}_{j,p} + \sum_i J_2 \vec{S}_{i,p} \cdot \vec{S}_{i,p+1} \\ & + \sum_{\langle\langle i,j,k \rangle\rangle} \left(J_3 \vec{S}_{i,p} \cdot \vec{S}_{j,p+1} + J_4 \vec{S}_{i,p} \cdot \vec{S}_{k,p+1} \right) \\ & + D \sum_i S^z_{i,p} S^z_{i,p} - g\mu_B \vec{H} \cdot \sum_i \vec{S}_{i,p}.\end{aligned}$$

As shown in figure 2(E), $J_1 > 0$ is the intraplane nearest-neighbor coupling constant (yellow bonds), J_2 represents the interplane nearest-neighbor coupling constant (red bonds), while J_3 (green bonds) and J_4 (blue bonds) correspond to two different next-nearest-neighbor interplane coupling constants. $D > 0$ is the single-ion anisotropy constant, and $\vec{H}$ is the external magnetic field. Indices p label the crystal plane, indices *i and j* indicate sites on the triangular lattice, with $\langle \ldots \rangle$ indicating summation over nearest neighbors. Similarly, *i, j*, and k label sites on the triangular layers, with $\langle \ldots \rangle$ denoting summation over interplane interactions. In this study, we used the reported values of $J_1 = 0.086$ meV and $D = 0.027$ meV for the isostructural compound $RbFe(MoO_4)_2$, which were determined by inelastic neutron scattering [12]. For our calculations, we set $J_2 = 0.005$ meV, $J_3 = 0.001$ meV, and $J_4 = 0.00128$ meV. By minimizing the magnetic energy, we optimized the magnetic structure of $RbFe(SO_4)_2$ in the absence of a magnetic field. The optimized structure is a chiral helical state with a propagation vector of (1/3, 1/3, 0.43), which closely matches our previous neutron diffraction results below 4 K. This agreement indicates that the exchange coupling constants we adopted for $RbFe(SO_4)_2$ are reasonable. Furthermore, we employed the Monte Carlo method based on the Metropolis–Hastings algorithm to calculate the temperature dependence of the specific heat of $RbFe(SO_4)_2$ [22]. The calculated results, shown in the inset of figure 2(B), exhibit a clear peak at 4 K, consistent with the Néel temperature determined from the χ–T curve. This further supports the validity of the exchange coupling constants used in our model. Next, we applied magnetic fields of 6.5 T and 13 T along the a-axis and optimized the corresponding magnetic structures. The results, displayed in figures 2(F) and (G), are in good agreement with our proposed magnetic structures for Phase II and Phase III, as shown in the inset of figure 2(C). Our calculations thus confirm that the proposed magnetic structures for Phase II and Phase III are reasonable.

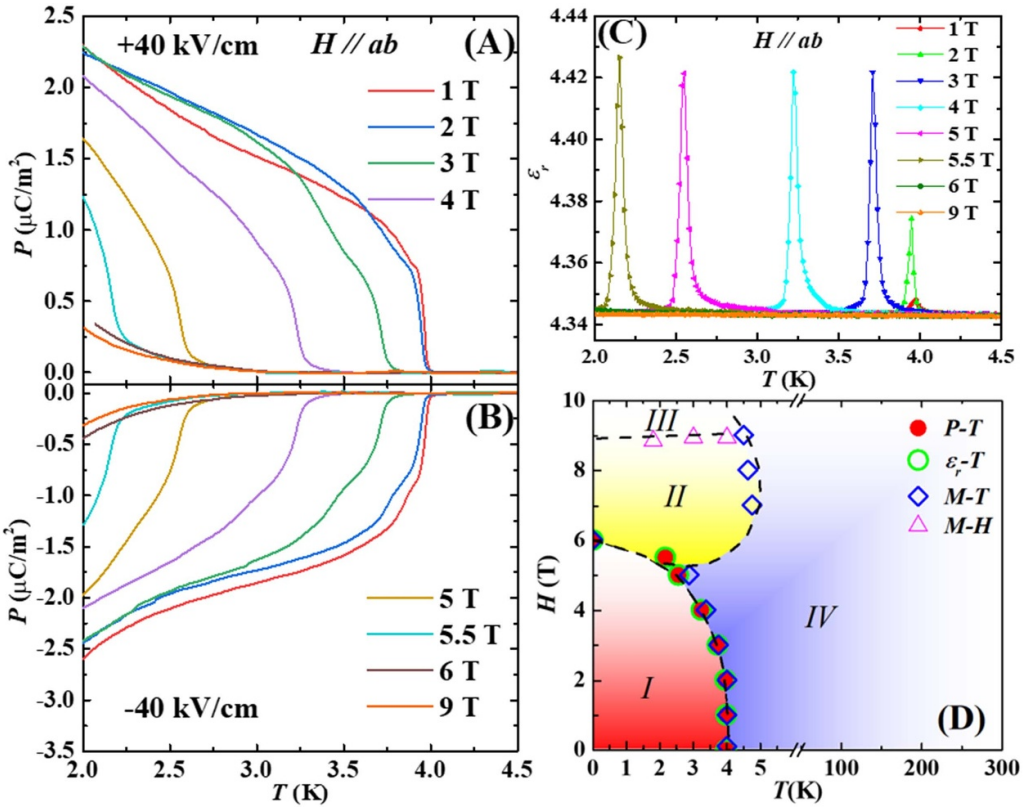

Figure 3. (A) Electric polarization as a function of temperature (P–T) measured under various magnetic fields, with a $+40$ kV cm^{-1} poling field. Magnetic fields were applied along the ab plane. (B) P–T curves measured under various magnetic fields, with a -40 kV cm^{-1} poling field. Magnetic fields were applied along the *ab* plane. (C) Dielectric constant as a function of temperature (ε_r–T) measured under various magnetic fields, with magnetic fields applied along the *ab* plane. (D) H–T phase diagram of $RbFe(SO_4)_2$, showing four distinct regions: I, II, III, and IV.

In our previous work, we reported that $RbFe(SO_4)_2$ exhibits ferroelectric polarization below 4 K and a dielectric peak at 4 K, both at zero external magnetic field [13]. The ferroelectric polarization arises due to a key permutable Symmetry Operational Similarity (SOS) relationship, expressed as $\mathcal{A} \cdot \mathcal{C} = \mathcal{P}$[23]. Here, $\mathcal{A}$ represents the ferro-rotational vector, $\mathcal{C}$ denotes chirality, and $\mathcal{P}$ corresponds to electric polarization. This relationship indicates that when a ferro-rotational object $\mathcal{A}$ interacts with chirality $\mathcal{C}$ (such as a chiral helical magnetic structure), the resultant $\mathcal{A} \cdot \mathcal{C}$ response manifests as an electric polarization $\mathcal{P}$. It also suggests that if the magnetic structure loses its chirality, the ferroelectricity could be suppressed. As suggested by the results in figure 2, when external magnetic fields are applied along the *ab* plane of $RbFe(SO_4)_2$, the chiral helical magnetic structure may be distorted into an achiral structure, implying that the ferroelectric transition in $RbFe(SO_4)_2$ could also be suppressed.

To confirm the effects of magnetic fields on the ferroelectricity of $RbFe(SO_4)_2$, we measured the electric polarization P along the c-axis of a $RbFe(SO_4)_2$ crystal as a function of temperature (P–T) under various magnetic fields. Before the measurements, the crystal was poled by an external electric field during the cooling process. Figure 3(A) shows the P–T curves obtained under a positive poling field of $+40$ kV cm^{-1}. At 1 T, consistent with the onset of helical magnetic order, P begins to increase at the ferroelectric transition temperature (T_{FE}) of ~ 4 K. As the magnetic field increases, T_{FE} gradually decreases, and the ferroelectric phase transition is no longer visible below 2 K when $H > 6$ T. To test the switchability of P, the P–T curve was also measured under a negative poling field of -40 kV cm^{-1}. As shown in figure 3(B), the polarization P is symmetric and switchable, and the ferroelectric phase transition disappears when $H > 6$ T. These observations strongly support the idea that the ferroelectricity of $RbFe(SO_4)_2$ arises from the interplay between magnetic chirality and ferro-rotational order. When the magnetic field exceeds 6 T, the chiral helical magnetic structure becomes achiral, leading to the disappearance of ferroelectricity. We also measured the temperature dependence of the dielectric constant ε_r. Figure 3(C) shows ε_r as a function of temperature (ε_r–T). At 1 T, a peak is observed slightly below 4 K in the ε_r–T curve. With increasing magnetic field, this peak shifts to lower temperatures and disappears above 2 K when $H \geqslant 6$ T, indicating a transition from the ferroelectric, chiral helical magnetic phase I to the paraelectric, achiral ferrimagnetic phase II.

The results of the P–T, M–T, M–H, and ε_r–T curves are summarized in the H–T phase diagram shown in figure 3(D). Four distinct regions are clearly revealed. At low magnetic fields and high temperatures ($T > 4$ K), the system is in the paramagnetic and paraelectric phase (IV). At low magnetic

fields ($H < 6$ T) and low temperatures ($T < 4$ K), it is in the chiral helical magnetic and ferroelectric phase (I). Between 6 and 9 T, and below 5 K, the system transitions into the collinear ferrimagnetic and paraelectric phase (II). For magnetic fields $H > 9$ T and below 5 K, the system enters the achiral noncollinear magnetic and paraelectric phase (III).

3. Conclusions

In this work, we report the structural, multiferroic, and magnetic properties, as well as the phase diagram of $RbFe(SO_4)_2$, a material that has not been extensively studied. Infrared absorption and Raman spectroscopy confirm the centrosymmetric nature of the ferro-rotational phase of $RbFe(SO_4)_2$ at room temperature. Neutron diffraction experiments on the nuclear peaks reveal significant thermal contraction of the lattice and confirm the absence of any long-range structural phase transition in $RbFe(SO_4)_2$ from 300 to 5 K. At $T > 150$ K, χ–T measurements show that $RbFe(SO_4)_2$ is an ideal 2D triangular antiferromagnetic lattice. At low temperatures, χ–T, along with P–T and ε_r–T measurements under various magnetic fields, reveal four distinct phases in the H–T phase diagram: (I) a ferroelectric and magnetic chiral helical phase below 4 K and 6 T, (II) a paraelectric and magnetic collinear phase below 4 K and above 6 T, (III) a paraelectric and magnetic non-collinear phase below 4 K and above 9 T, and (IV) a paraelectric and paramagnetic phase above 4 K. M–H measurements at 1.8 K indicate that as the magnetic field increases, the chiral helical magnetic structure transitions to a collinear achiral magnetic structure at 6 T, followed by the appearance of a plateau between 6 and 9 T. Above 9 T, the magnetic structure likely transitions to an achiral, non-collinear configuration. This study advances our understanding of the structural properties, multiferroic properties, magnetic transitions under magnetic fields, and the H–T phase diagram of $RbFe(SO_4)_2$, providing valuable insights into the exotic physical properties of this ferro-rotational magnet.

4. Experimental section

Single crystals of $RbFe(SO_4)_2$ were synthesized using the hydrothermal method in a 50 ml Teflon-lined autoclave at 483 K [13]. The M–T curves were measured using a 9 T Cryogen Free Measurement System (Cryogenic Limited), and the M–H curves were measured using a 14 T Physical Property Measurement System (Quantum Design). The dielectric constant was determined at 1 kHz using an LCR meter (Keysight E4980AL) and ferroelectric polarization was measured by the pyro-current method with an electrometer (Keithley 6517B). Neutron diffraction experiments were conducted at the BT4 triple-axis spectrometer (with a 2.36 Å wavelength) at the NIST Center for Neutron Research. The optimization of the magnetic structure and the Monte Carlo simulation of the specific heat were performed using the Metropolis–Hastings algorithm with the SpinW package [22].

Data availability statement

All data that support the findings of this study are included within the article (and any supplementary files).

Acknowledgment

J Y acknowledges support by DOE under Grant No. DOE: DE-SC0021188. J L M acknowledges support by NSF CMP (DMR-2226109). S Y is financially supported by the National Science and Technology Council of Taiwan, with Grant Nos. 112-2112-M-213-019 and 113-2112-M-213-011. The work at the University of Michigan is supported by the Department of Energy under Award No. DE-SC0020184 for the magnetization measurements. Any mention of commercial products is for information only; it does not imply recommendation or endorsement by NIST.

ORCID iDs

Junjie Yang https://orcid.org/0000-0001-6337-3531
William Ratcliff https://orcid.org/0000-0001-8956-3851
Lu Li https://orcid.org/0000-0002-8054-7406
Shinichiro Yano https://orcid.org/0000-0003-0034-8931

References

[1] Hearmon A J, Fabrizi F, Chapon L C, Johnson R D, Prabhakaran D, Streltsov S V, Brown P J and Radaelli P G 2012 Electric field control of the magnetic chiralities in ferroaxial multiferroic $RbFe(MoO_4)_2$ *Phys. Rev. Lett.* **108** 237201

[2] Johnson R D, Chapon L C, Khalyavin D D, Manuel P, Radaelli G and Martin C 2012 Giant improper ferroelectricity in the ferroaxial magnet $CaMn_7O_{12}$ *Phys. Rev. Lett.* **108** 067201

[3] Hlinka J, Privratska J, Ondrejkovic P and Janovec V 2016 Symmetry guide to ferroaxial transitions *Phys. Rev. Lett.* **116** 177602

[4] Hayashida T, Uemura Y, Kimura K, Matsuoka S, Morikawa D, Hirose S, Tsuda K, Hasegawa T and Kimura T 2020 Visualization of ferroaxial domains in an order-disorder type ferroaxial crystal *Nat. Commun.* **11** 124409

[5] Jin W, Drueke E, Li S, Admasu A, Owen R, Day M, Sun K, Cheong S W and Zhao L 2020 Observation of a ferro-rotational order coupled with second-order nonlinear optical fields *Nat. Phys.* **16** 42–46

[6] Hayashida T, Uemura Y, Kimura K, Matsuoka S, Hagihala M, Hirose S, Morioka H, Hasegawa T and Kimura T 2021 Phase transition and domain formation in ferroaxial crystals *Phys. Rev. Mater.* **5** 124409

[7] Luo X, Obeysekera D, Won C, Sung S H, Schnitzer N, Hovden R, Cheong S W, Yang J, Sun K and Zhao L 2021 Ultrafast modulations and detection of a ferro-rotational charge density wave using time-resolved electric quadrupole second harmonic generation *Phys. Rev. Lett.* **127** 126401

[8] Owen R, Drueke E, Albunio C, Kaczmarek A, Jin W, Obeysekera D, Cheong S W, Yang J, Cundiff S and Zhao L 2021 Second-order nonlinear optical and linear ultraviolet-visible absorption properties of the type-II multiferroic candidates $RbFe(AO_4)_2$ (A = Mo,Se, S) *Phys. Rev.* B **103** 054104

[9] Guo X *et al* 2023 Ferrorotational domain walls revealed by electric quadrupole second harmonic generation microscopy *Phys. Rev.* B **107** L180102
[10] Jin W 2023 Voltage enables ferro-rotational domain switching *Nat. Nanotechnol.* **18** 840
[11] Liu G *et al* 2023 Electrical switching of ferro-rotational order in nanometre-thick 1T-TaS_2 crystals *Nat. Nanotechnol.* **18** 854
[12] White J S, Niedermayer C, Gasparovic G, Broholm C, Park J M S, Shapiro A Y, Demianets L A and Kenzelmann M 2013 Multiferroicity in the generic easy-plane triangular lattice antiferromagnet $RbFe(MoO_4)_2$ *Phys. Rev.* B **88** 060409(R)
[13] Yang J *et al* 2024 Electric-field manipulation of magnetic chirality in a homo-ferro-rotational helimagnet *Adv. Sci.* **11** 2402048
[14] Fan S *et al* 2021 Excitations of intercalated metal monolayers in transition metal dichalcogenides *Nano Lett.* **21** 99–106
[15] Nihira T and Iwata T 2003 Temperature dependence of lattice vibrations and analysis of the specific heat of graphite *Phys. Rev.* B **68** 134305
[16] Klimin S A *et al* 2003 Structural phase transition in the two-dimensional triangular lattice antiferromagnet $RbFe(MoO_4)_2$ *Phys. Rev.* B **68** 174408
[17] Bazarov B G, Namsaraeva T V, Klevtsova R F, Anshits A G, Vereshchagina T A, Glinskaya L A, Fedorov K N and Bazarova Z G 2010 Growth and crystal structure of binary molybdate $CsFe(MoO_4)_2$ *Crystallogr. Rep.* **55** 591–3
[18] Cao K, Johnson R D, Giustino F, Radaelli P G, Guo G C and He L 2014 First-principles study of multiferroic $RbFe(MoO_4)_2$ *Phys. Rev.* B **90** 024402
[19] Mitamura H *et al* 2014 Spin-chirality-driven ferroelectricity on a perfect triangular lattice antiferromagnet *Phys. Rev. Lett.* **113** 147202
[20] Chubokov A V and Golosov D I 1991 Quantum theory of an antiferromagnet on a triangular lattice in a magnetic field *J. Phys.: Condens. Matter* **3** 69–82
[21] Zhitomirsky M E 2014 Real-space perturbation theory for frustrated magnets: application to magnetization plateaus *J. Phys.: Conf. Ser.* **592** 012110
[22] Toth S and Lake B 2015 Linear spin wave theory for single-Q incommensurate magnetic structures *J. Phys.: Condens. Matter* **27** 166002
[23] Cheong S W, Lim S, Du K and Huang F T 2021 Permutable SOS (symmetry operational similarity) *npj Quantum Mater.* **6** 58